



CHORUS

This is the accepted manuscript made available via CHORUS. The article has been published as:

Origin of finite pulse trains: Homoclinic snaking in excitable media

Arik Yochelis, Edgar Knobloch, and Michael H. Köpf
Phys. Rev. E **91**, 032924 — Published 25 March 2015

DOI: [10.1103/PhysRevE.91.032924](https://doi.org/10.1103/PhysRevE.91.032924)

The origin of finite pulse trains: Homoclinic snaking in excitable media

Arik Yochelis,¹ Edgar Knobloch,² and Michael H. Köpf³

¹*Department of Solar Energy and Environmental Physics,
Swiss Institute for Dryland Environmental and Energy Research,
Jacob Blaustein Institutes for Desert Research (BIDR), Ben-Gurion University of the Negev,
Sede Boqer Campus, Midreshet Ben-Gurion 84990, Israel**

²*Department of Physics, University of California, Berkeley, CA 94720, USA*

³*Département de Physique, École Normale Supérieure, 24 rue Lhomond, 75005 Paris, France*

(Received March 12, 2015)

Many physical, chemical and biological systems exhibit traveling waves as a result of either an oscillatory instability or excitability. The latter may admit a large multiplicity of stable and spatially localized wavetrains consisting of different numbers of traveling pulses. The existence of these states is related here to the presence of homoclinic snaking in the vicinity of a subcritical, finite wavenumber Hopf bifurcation. The pulses are organized in a slanted snaking structure resulting from the presence of a heteroclinic cycle between small and large amplitude traveling waves. Connections of this type require a multivalued dispersion relation. This dispersion relation is computed numerically and used to interpret the profile of the pulse group. The different spatially localized pulse trains can be accessed by appropriately customised initial stimuli thereby blurring the traditional distinction between oscillatory and excitable systems. The results reveal a new class of phenomena relevant to spatiotemporal dynamics of excitable media, particularly in chemical and biological systems with multiple activators and inhibitors.

PACS numbers: 47.54.-r, 47.20.Ky, 47.35.Fg, 82.40.Ck

I. INTRODUCTION

Excitability is frequently observed in systems driven far from equilibrium [1–3]. Examples include biological systems [4, 5], autocatalytic chemical reactions [6, 7], electrochemistry [8], liquid crystals [9], nonlinear optics [10], semiconductors [11–13], and pipe flow [14]. A spatially extended system with a stable spatially uniform equilibrium state is called excitable when a large enough, spatially localized perturbation excites adjacent sites while the perturbation at the original location decays back to equilibrium. The resulting dynamics then takes the form of a spatially localized excitation that propagates away from the initial disturbance. In higher space dimensions, excitability may lead to complex spatiotemporal behavior including formation and breakup of spiral waves [1–3, 6, 7], a process detrimental to the functioning of the heart [15].

The basic properties of excitable systems are well described by two-variable reaction-diffusion equations of FitzHugh-Nagumo (FHN) type [16–18]. However, chemical and biological systems often involve a large number of reacting and diffusing components, making it difficult to differentiate between oscillatory and excitable dynamics and the effects of intrinsic fluctuations [19–21]. A proper theoretical framework capturing this complexity within a minimal model is therefore essential. In the area of excitable systems recent work has demonstrated that a number of observed phenomena, including spiral wave coarsening [22], pulse/spot interactions [23–25] and prop-

agating oscillons [26] can only be captured within three-variable models. Such models are also capable of describing the generation of stable finite pulse trains consisting of different numbers of pulses using appropriately customized initial conditions [27], a behavior heretofore unknown in excitable media with local interactions [28, 29]. In this paper we show that the mechanism responsible for the presence of a large multiplicity of different traveling pulse trains is related to a phenomenon known as *homoclinic snaking* [30] that has hitherto been observed only for stationary pulses in the vicinity of subcritical Turing-type instabilities [30–33].

II. FINITE WAVENUMBER HOPF INSTABILITY IN A THREE-VARIABLE REACTION-DIFFUSION MODEL

We employ a simple three-variable but local extension of the prototypical FHN model [34]:

$$\frac{\partial u}{\partial t} = u - u^3 - v + D \frac{\partial^2 u}{\partial x^2}, \quad (1a)$$

$$\epsilon \frac{\partial v}{\partial t} = u - a_v v - a_w w - a_0, \quad (1b)$$

$$\frac{\partial w}{\partial t} = u - w + \frac{\partial^2 w}{\partial x^2}. \quad (1c)$$

Here the new field $w(x, t)$ controls the inhibitor $v(x, t)$ and as such can be regarded as a second activator, in addition to the activator $u(x, t)$. In contrast to the standard two-variable FHN model (i.e., $a_w = 0$) the spatially uniform state in the three-variable system (1) may undergo a finite-wavenumber Hopf instability [27, 35, 36].

* yochelis@bgu.ac.il

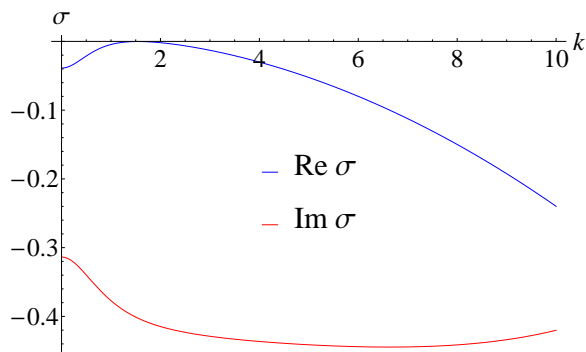


FIG. 1. (Color online) Real (dark/blue line) and (negative) imaginary (light/red line) parts of the dispersion relation $\sigma(k)$ computed from a linear analysis of Eqs. (1) at the instability onset $a_v = a_v^{Hopf}$.

On periodic domains with period equal to the critical wavelength this instability generates two types of time-dependent states: traveling waves (hereafter TW) and standing waves (hereafter SW).

In the following we use a_v as a control parameter and keep $a_w = 0.5$, $\epsilon = 5$, $a_0 = -0.1$, $D = 0.005$ fixed. With this parameter choice, the system (1) has a single spatially uniform equilibrium $\vec{U}_0 \equiv (u_0, v_0, w_0)$ for $a_v \lesssim 0.8919$. Linear stability analysis,

$$\begin{pmatrix} u \\ v \\ w \end{pmatrix} - \begin{pmatrix} u_0 \\ v_0 \\ w_0 \end{pmatrix} \propto e^{\sigma t + ikx}, \quad (2)$$

shows that as a_v decreases, \vec{U}_0 undergoes a finite-wavenumber Hopf instability: $\text{Re}[\sigma(k = k_c)] = 0$, $\text{Re}[\sigma(k \neq k_c)] < 0$, $\text{Im}[\sigma(k = k_c)] \equiv \pm\omega_c \neq 0$ at $a_v = a_v^{Hopf} \simeq 0.4497$. The real and (negative) imaginary parts of the dispersion relation at $a_v = 0.4497$ are shown in Fig. 1 and reveal that the critical wavenumber $k_c \simeq 1.546$ and the critical frequency $\omega_c \simeq -0.4$ (right-traveling waves).

To determine the TW and SW branches emanating from $a_v = a_v^{Hopf}$ we proceed as follows. The TW solutions are computed numerically in a comoving frame, $\xi \equiv x - ct$, in which they are stationary. In this frame stationary solutions solve a set of five first order ODEs,

$$\frac{du}{d\xi} = h, \quad (3a)$$

$$D \frac{dh}{d\xi} = -(ch + u - u^3 - v), \quad (3b)$$

$$c\epsilon \frac{dv}{d\xi} = -(u - a_v v - a_w w - a_0), \quad (3c)$$

$$\frac{dw}{d\xi} = r, \quad (3d)$$

$$\frac{dr}{d\xi} = -(cr + u - w). \quad (3e)$$

These equations are solved on a periodic domain with period $2\pi/k_c$ using the continuation package AUTO [37]

starting from small amplitude oscillations for $a_v \approx a_v^{Hopf}$ and incrementing the parameter a_v . The computation requires the solution of a nonlinear eigenvalue problem for the speed c of the TW since this speed depends on the TW amplitude. Temporal stability of the resulting solutions is calculated via a standard eigenvalue numerical method using the time-dependent version of Eqs. (1) in the appropriate comoving frame. The resulting TW branch is shown using a light/red line in Fig. 2. Both weakly nonlinear theory (not shown) and numerical continuation show that the TW branch bifurcates subcritically (i.e., towards larger a_v) before turning around in a fold labeled a_v^{SN} ; the upper branch TW are initially unstable with respect to long wavelength perturbations (dashed light/red line) but acquire stability for $a_v \lesssim 0.5$ (solid light/red line).

The computation of the SW branch (dark/blue line in Fig. 2) requires a different approach. For SW, we solve simultaneously (using AUTO) a set of ODEs at each individual spatial grid point, $x_i = i\Delta x \in [0, 2\pi/k_c]$, generated by a finite difference spatial discretization, while adding a very small gradient, $\delta \sim 10^{-8}$, to one of the fields to destroy the invariance of the SW with respect to translations that is present with periodic boundary conditions:

$$\begin{aligned} \frac{\partial u_i}{\partial t} &= u_i - u_i^3 - v_i + D \frac{u_{i+1} + u_{i-1} - 2u_i}{\Delta x^2} \\ &\quad + \delta \frac{u_{i+1} - u_{i-1}}{2\Delta x}, \end{aligned} \quad (4a)$$

$$\epsilon \frac{\partial v_i}{\partial t} = u_i - a_v v_i - a_w w_i - a_0, \quad (4b)$$

$$\frac{\partial w_i}{\partial t} = u_i - w_i + \frac{w_{i+1} + w_{i-1} - 2w_i}{\Delta x^2}. \quad (4c)$$

Figure 2 shows that the SW also bifurcate subcritically. Stability calculations near onset indicate that on a periodic domain with period $2\pi/k_c$ the TW are once unstable while the SW are twice unstable, i.e., the SW are unstable with respect to TW perturbations [38]. As a result the SW state remains unstable throughout (dashed dark/blue line).

III. FINITE PULSE TRAINS AND HOMOCLINIC SNAKING

With increasing amplitude the speed c of the TW first decreases and then increases as the TW branch turns around towards smaller a_v , producing a region of bistability between the homogeneous equilibrium \vec{U}_0 and slower, stable, large-amplitude TW [solid black line in Fig. 3(a)]. In this regime the system also admits a series of coexisting stable spatially *localized* traveling pulses [27], hereafter referred to as slow and fast pulses according to their speed relative to the TW [Fig. 3(a)]. These also solve Eqs. (3) but now on large periodic domains. Of these, the slow pulses are unstable in the context of Eqs. (1) with reflecting boundary conditions at $x = 0, L$, and

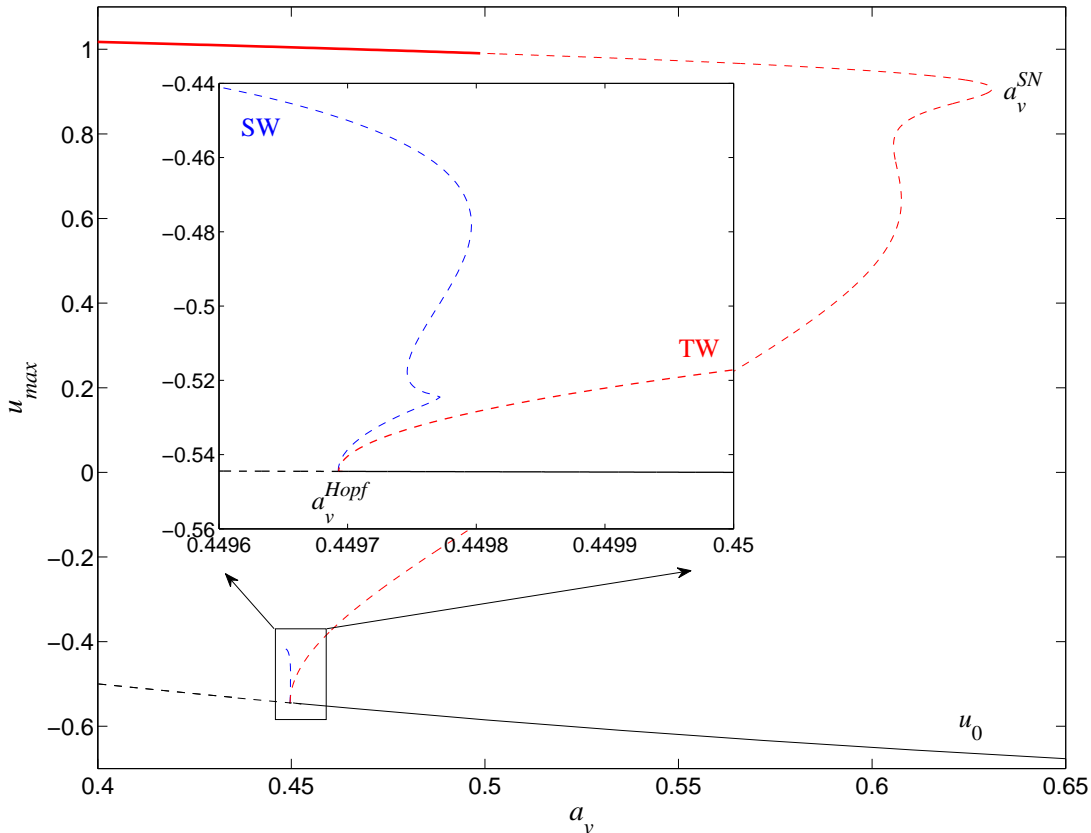


FIG. 2. (Color online) Bifurcation diagram showing branches of standing (SW, blue/dark line) and traveling (TW, red/light line) waves in terms of the maximum value u_{max} of the u field, obtained via numerical continuation; the solid red/light line indicates TW that are linearly stable with respect to perturbations with arbitrary wavenumber. The solid black line indicates the stable uniform state u_0 . The finite wavenumber Hopf instability takes place at a_v^{Hopf} .

evolve quickly into fast pulses Ξ_1^1 , as shown via direct numerical integration of Eqs. (1) in Fig. 4. Figure 3 summarizes our numerical continuation results in a bifurcation diagram with a_v as parameter and the speed c as a measure of the amplitude of the solution. For other parameter values, e.g., $(a_0, a_v) = (-0.11, 0.5)$ instead of $(a_0, a_v) = (-0.1, 0.5)$, both pulse types are stable in 1D and 2D direct integration of Eqs. (1), as shown in Fig. 5.

As shown in Fig. 3(a), the slow and fast pulses are organized into families of traveling pulses labeled Ξ_m^n ($m = n, n + 1$), where the index n labels the family ($n = 1, 2$) and m refers to the number of pulses. The figure shows two such families lying on closed curves or *isolas* [39] in the (a_v, c) plane, one of which (dark/blue) is based on a single fast pulse state ($n = 1, m = 1$), while the other (light/red) is based on a two-pulse state ($n = 2, m = 2$); the index $m = n$ along the left segment of each branch and changes to $m = n + 1$ at saddle nodes on the left where an extra *trailing* pulse is added [Fig. 3(b), right panel] before the branch ‘returns’ to the same region of the (a_v, c) plane. Figure 3(a) shows that

this extra pulse differs in profile from the existing pulses and is separated from them by a larger distance. Numerical computation shows that the region near the diamond symbol in Fig. 3(a) is filled with branches of stable and unstable multipulse states, all of which lie on isolas of this type and all of which travel with essentially indistinguishable speeds ($c \simeq 0.25$ at $a_v = 0.5$).

To examine the origin of these isolas we show in the left panel of Fig. 3(b) an enlargement of the branches of fast pulses as they approach the unstable small amplitude TW branch near $a_v \approx 0.4515 > a_v^{Hopf}$. This enlargement is replotted in Fig. 6 in terms of the norm

$$N \equiv \sqrt{\frac{1}{L} \int_0^L (u^2 + v^2 + w^2 + u_\xi^2 + w_\xi^2) d\xi}, \quad (5)$$

where L is the domain period. As one follows the Ξ_1^1 branch towards larger N (smaller c) it undergoes repeated back and forth excursions, adding one pulse at the *leading* edge per excursion (Fig. 6), in a manner reminiscent of homoclinic snaking [30] in spatially reversible sys-

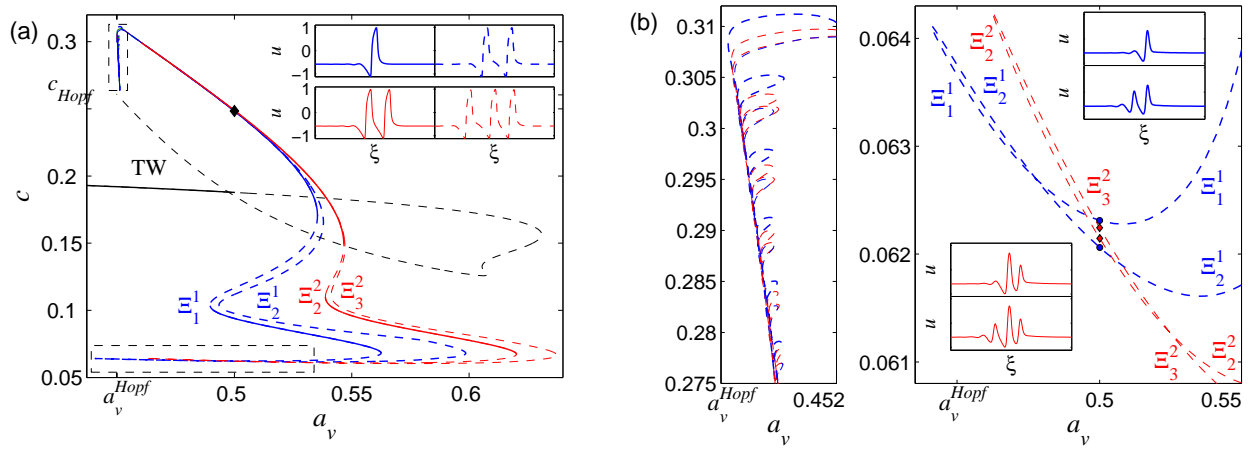


FIG. 3. (Color online) (a) Bifurcation diagram for the Ξ_m^1 [$m = 1, 2$, thick (dark/blue) line] and Ξ_m^2 [$m = 2, 3$, thin (light/red) line] pulse branches and the traveling wave (TW) branch showing the speed c as a function of a_v on a periodic domain with period $L = 300$, where m indicates the number of pulses in the wave train. The Ξ_1^1 and Ξ_2^1 branches connect at the leftmost saddle node where a trailing pulse is added, and similarly for Ξ_2^2 and Ξ_3^2 . The insets show the profiles $u(\xi)$, $\xi \in [0, 20]$, at $a_v = 0.5$, $c \approx 0.25$, corresponding to the diamond symbol. The Hopf bifurcation occurs at $a_v = a_v^{Hopf} \approx 0.4497$, $c \approx 0.26$. (b) Left panel: Zoom of the $\Xi_{1,2}^1$ and $\Xi_{2,3}^2$ snaking region [top rectangle in (a)]. Right panel: Zoom of the leftmost saddle node region [bottom rectangle in (a)]. The insets show profiles $u(\xi)$ for $\xi \in [0, 10]$ at $a_v = 0.5$ on the same scale as in (a). Solid (dashed) lines indicate pulse solutions that are stable (unstable) with respect to perturbations of wavelength L ; they also indicate the stability of the TW with respect to all perturbations with wavelength $\lambda \geq \lambda_c \equiv 2\pi/k_c$.

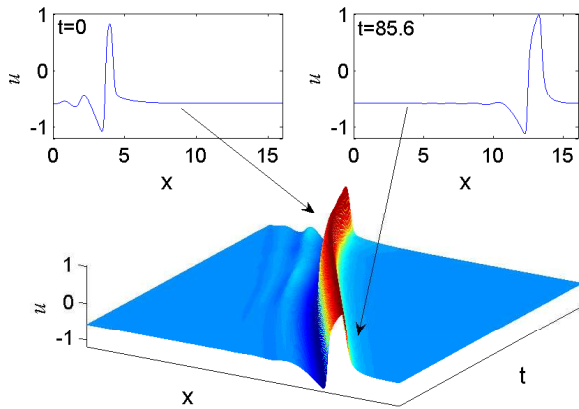


FIG. 4. (Color online) Decay of a slow Ξ_1^1 pulse with $c \approx 0.09$ into a fast Ξ_1^1 pulse with $c \approx 0.25$ (black diamond in Fig. 3(a)) when $a_v = 0.5$.

tems with broken spatial reflection symmetry [40]. Each of the resulting multipulse states is embedded in a TW background [Fig. 6, insets (a,b)], and the same behavior is found on the ‘returning’ Ξ_2^1 branch with its extra but different trailing pulse [insets (c,d)]. Identical behavior obtains for the $n > 1$ isolas and is independent of the domain size, as long as $L \gg 2\pi/k_c$. Figure 6 reveals a marked difference in amplitude between the small and large amplitude traveling waves indicating that, for the parameter values used here, the system is far from the transition from supercritical to subcritical branching that is responsible for the presence of localized states near subcritical Turing bifurcations [41]. The inclination

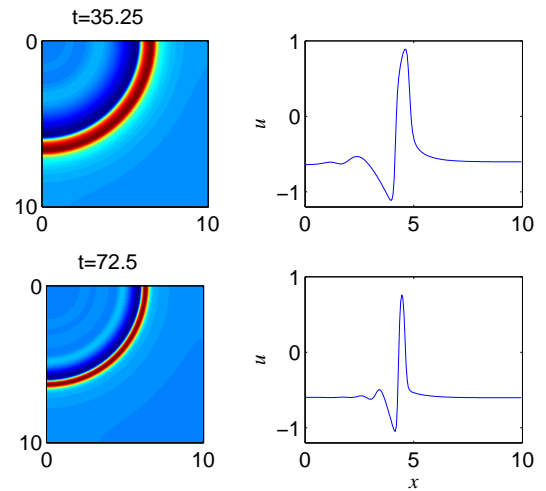


FIG. 5. (Color online) 2D and 1D solutions to Eqs. (1) with reflecting boundary conditions, showing coexistence of stable fast (top two panels) and stable slow (bottom two panels) Ξ_1^1 pulses when $a_v = 0.5$ and $a_0 = -0.11$.

of the snaking structure is a consequence of the nonlocal nature of the eigenvalue problem for the speed c of the pulse train, cf. [42–44], but disappears near the heteroclinic cycle. This is a consequence of the fact that as N increases the behavior shown in Fig. 6 (top panel) accumulates at a finite value of a_v , viz., $a_v \approx 0.4515$.

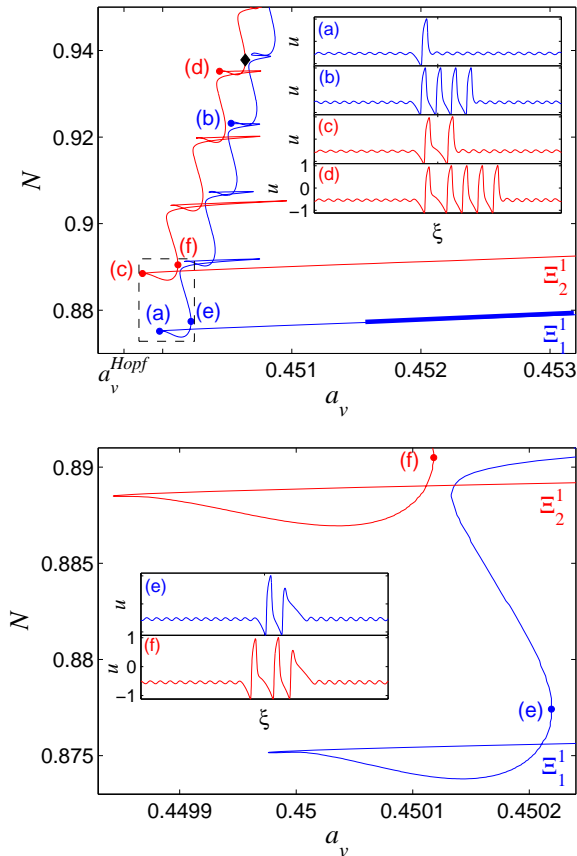


FIG. 6. (Color online) Top panel: Bifurcation diagram for the Ξ_m^1 ($m = 1, 2$) pulse branches; the insets correspond to locations indicated in the diagram. The waves travel from left to right. An ‘extra’ trailing pulse is present along the Ξ_2^1 branch. Bottom panel: Zoom of the bottom leftmost region of the top panel [dashed rectangle] showing the nucleation of the leading pulse. The profiles are shown for $\xi \in [0, 120]$ but are computed on a domain of size $L = 300$; the amplitude scale for u is the same as in Fig. 3(a).

A. Heteroclinic cycle

The behavior shown in Fig. 6 appears to be associated with the formation at $a_v \approx 0.4515 > a_v^{Hopf}$ of a heteroclinic cycle between small and large amplitude periodic traveling waves, i.e., the formation of a pair of fronts, one connecting the small amplitude TW to the large amplitude TW while the other connects the large amplitude TW to the small amplitude TW, as demonstrated in Fig. 7. This cycle is of codimension one since the latter connection is structurally stable, cf. [45]. In contrast, the finite pulse trains constructed in [46] for the two-variable FHN model correspond to the existence of multipulse homoclinics near a primary homoclinic orbit of Shil’nikov type [47]; in such pulse trains the individual pulses are widely separated instead of forming a cluster [48].

The approach to the heteroclinic cycle occurs via the repeated nucleation of new pulses at the *front* of the

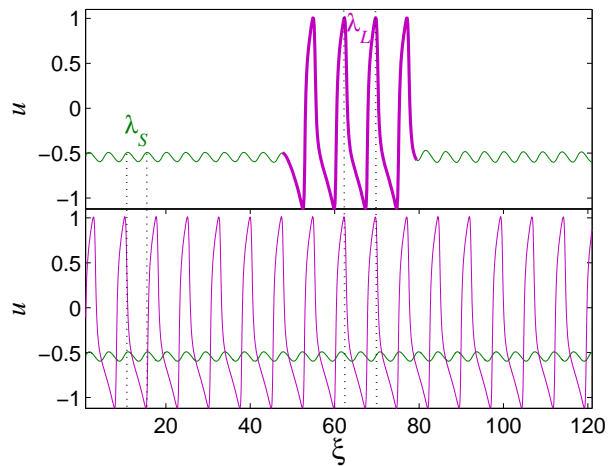


FIG. 7. (Color online) A four-pulse train and TW profiles at $a_v \approx 0.450358$, corresponding to the saddle node (b) in Fig. 6 (top panel). The dotted lines correspond to one wavelength of the coexisting small amplitude (λ_S) and large amplitude (λ_L) TW. These wavelengths are precisely the wavelengths present in the pulse train in the top panel.

pulse train, resulting in the formation of ever longer pulse trains embedded in a small amplitude TW background (Fig. 6). Since the fronts connect a stable large amplitude TW to an unstable small amplitude TW, the multipulse states created via this process are unstable; simulations reveal that they evolve into large amplitude TW. However, with increasing a_v the pulse trains acquire stability, as indicated in Fig. 3(a).

Owing to the nonlinearity of the problem the two coexisting TW have different wavelengths, hereafter denoted by λ_S and λ_L , respectively (Fig. 7) and, in general, travel with different phase speeds c_S and c_L . However, in order that the resulting heteroclinic cycle be stationary in a moving frame it is necessary that both TW travel with the same speed c , i.e., $c_S = c_L = c$. In addition, since the pulse train travels to the right the two *fronts* at either side cannot be related by the reflection symmetry $\xi \rightarrow -\xi$ as in spatially reversible systems. Consequently, the fronts are associated with distinct wavelengths, λ_f at the front and λ_r at the rear, which differ in general from $\lambda_{S,L}$.

B. Nonlinear dispersion relation

The requirement $c_S = c_L = c$ can only be satisfied in systems with a multivalued dispersion relation $\lambda(c)$, where λ is the TW wavelength, cf. [39, 49–53]. We emphasize that this wavelength is a continuous parameter and so can be selected at will, unlike the wave amplitude. Thus each wavelength is associated with a (locally) unique amplitude. The dispersion relation is determined numerically by computing the TW speed c in a domain with period λ and varying the wavelength λ ; the result

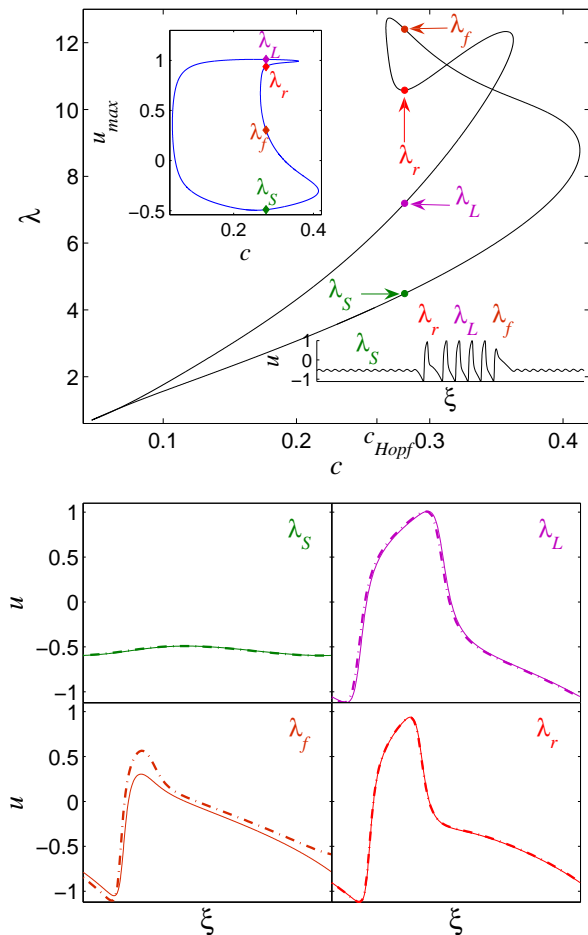


FIG. 8. (Color online) Top panel: nonlinear dispersion relation for TW at $a_v \simeq 0.45064$, corresponding to the location of a saddle node on the pulse train (shown for $\xi \in [0, 150]$ in the lower inset) that lies on the Ξ_2^1 branch [diamond symbol in Fig. 6 (top panel)]. The wavelengths $\lambda_S \simeq 4.488$, $\lambda_L \simeq 7.192$, $\lambda_f \simeq 12.406$, $\lambda_r \simeq 10.577$ are computed for $c \simeq 0.28116$ (the speed of the pulse train), with $\lambda_{f,r}$ corresponding to the wavelengths associated with the front and rear connections. The top inset shows the dispersion relation as u_{max} vs. c , and depicts the amplitudes of the different TW. The bottom panel compares the profiles over one period of each TW corresponding to the four different wavelengths (solid lines) identified in the top panel with the corresponding profile from within the pulse train (dashed-dotted lines) shown in the lower inset in the top panel.

is shown in Fig. 8 (top). The upper inset shows the corresponding amplitude u_{max} as a function of c while the lower inset shows a pulse train corresponding to the diamond symbol in Fig. 6 (top). To characterize this pulse train we take a vertical cut through the (c, λ) plane at $c \approx 0.28116$, the speed of this pulse train. The slice reveals the presence of four wavelengths, $\lambda_{S,L}$ corresponding to the pair of coexisting wavetrains, as well as $\lambda_{f,r}$ that manifest themselves in the front and rear connections only. Figure 8 (bottom) shows the profiles corre-

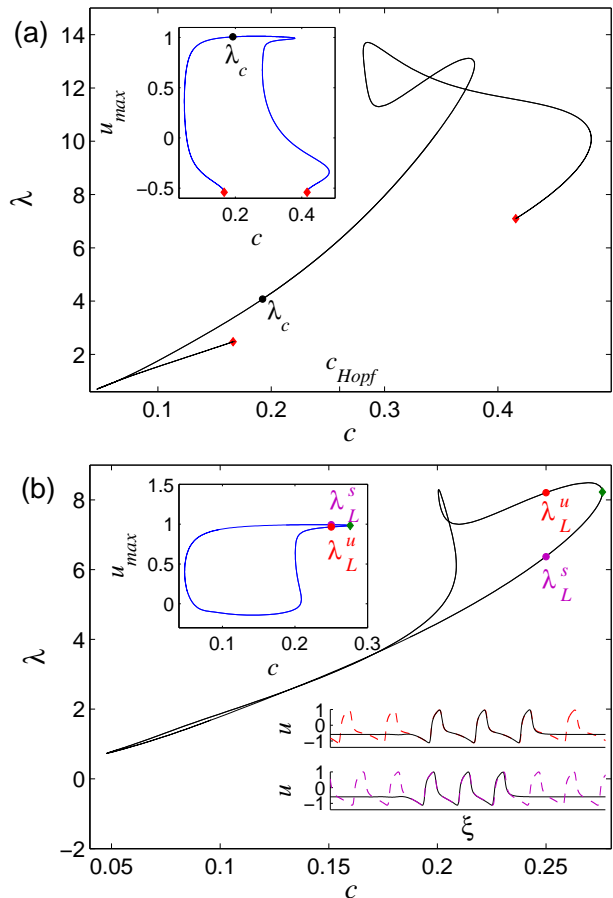


FIG. 9. (Color online) Nonlinear dispersion relation for TW at (a) $a_v = 0.445 < a_v^{Hopf}$ and (b) $a_v = 0.5 > a_v^{Hopf}$. The red diamond symbols in (a) indicate the wave numbers at which $\text{Re}[\sigma(k)] = 0$ (see Eq. (2)), i.e., the limits of the band of linearly unstable wave numbers around $k = k_c$ when $a_v < a_v^{Hopf}$ (cf. Fig. 1). Large amplitude TW with wavelength $\lambda_c \equiv 2\pi/k_c$ move with speed $c \simeq 0.1924$. The 3-pulse state in (b) corresponds to the stable solution on the Ξ_3^3 branch at $a_v = 0.5$ in Fig. 3 and travels with speed $c \simeq 0.25$ corresponding to two intersections with the nonlinear dispersion relation, $\lambda_L^s \simeq 6.3$ and $\lambda_L^u \simeq 8.2$. The periodic TW with these wavelengths are shown in the inset (for $\xi \in [0, 50]$) and are, respectively, stable (superscript s) and unstable (superscript u) with respect to perturbations with wavelength λ . The dispersion relation connects to a periodic TW with $\lambda_{TW} \simeq 8.225$, $c \simeq 0.276$ at the location indicated by the green diamond symbol.

sponding to each wavelength selected by this construction, obtained via numerical continuation, and demonstrates the matching of these profiles to the corresponding segments of the pulse train in Fig. 8 (top).

In Fig. 9(a,b) we show the corresponding results for $a_v = 0.445 < a_v^{Hopf}$ and $a_v = 0.5 > a_v^{Hopf}$, respectively. For $a_v < a_v^{Hopf}$ the small amplitude TW are absent and the dispersion relation accordingly opens up forming a gap from which the wavelength λ_S is absent, as shown in Fig. 9(a). In this parameter regime excitable pulses

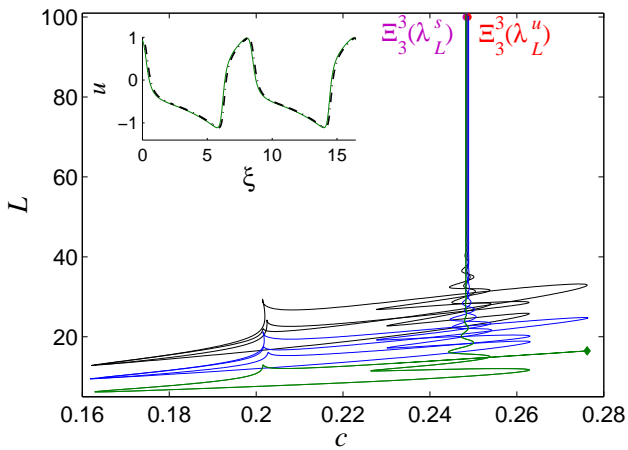


FIG. 10. (Color online) Nonlinear pulse dispersion relations at $a_v = 0.5$ computed by starting from the 3-pulse state (black line, bottom inset in Fig. 9(b)), 2-pulse state (blue/dark line) and a single-pulse state (green/light line), all in a domain of length $L = 100$. The green diamond symbol on the single-pulse branch indicates the termination of the branch of single pulse states ($L \simeq 16.45 \simeq 2\lambda_{TW}$) on the corresponding TW solution indicated in Fig. 9(b) and shown in a black dashed line in the inset, i.e., the green diamond represents a wavelength-doubling bifurcation of the periodic TW.

are absent since the uniform state is unstable and only TW with wavelength $\lambda \sim \lambda_c \equiv 2\pi/k_c \approx 4.07$ remain. In the regime $a_v^{Hopf} < a_v < 0.5$ where stable TW and finite pulse trains coexist, the nonlinear dispersion undergoes an important change as the background small amplitude TW disappear with increasing a_v . The resulting dispersion relation at $a_v = 0.5$ captures the profile of the finite pulse train of type Ξ_m^m , $m \geq 2$, at $c \simeq 0.25$ and in particular the two interpulse separations $\lambda_L^s \simeq 6.3$ [visible in the inset in Fig. 3(a)] and $\lambda_L^u \simeq 8.2$. Thus, the nonlinear dispersion relations are able to explain the profile of the finite pulse train both in the presence of the small amplitude traveling waves and in their absence.

Figure 10 shows the pulse dispersion relation obtained by varying the domain period L starting with 3-pulse, 2-pulse and 1-pulse states on a domain with relatively large period ($L = 100$) and decreasing L . The speed of these states remains fixed until L decreases below $L \sim 40$ for the 3-pulse state, and even smaller L for the 2- and 1-pulse states. Figure 9(b, inset) shows that there are in fact two distinct 3-pulse states based on the wavelengths $\lambda_L^s \simeq 6.3$ and $\lambda_L^u \simeq 8.2$ determined from the nonlinear dispersion relation obtained with $L = \lambda$; these are labeled $\Xi_3^3(\lambda_L^s)$ and $\Xi_3^3(\lambda_L^u)$, respectively. The speeds of these 3-pulse states are very close to one another and independent of L (when is L large, $L \gg 2\pi/k_c$), and this is so for the 2- and 1-pulse states as well. Figure 10 also shows that the single pulse branch terminates on the TW branch when $L \simeq 16.45 \simeq 2\lambda_{TW}$. This termination point coincides with the fold of the TW dispersion relation indicated by the green diamond symbol in Fig. 9(b), showing

that at this point a TW with period λ is unstable with respect to perturbations of a longer wavelength, in this case 2λ , representing a wavelength-doubling bifurcation.

Figure 11 sheds light on the evolution of the TW nonlinear dispersion relation with decreasing a_v (from $a_v = 0.5$ towards the snaking region) and uses the results to interpret changes in the profile of the 3-pulse state on the Ξ_3^3 branch as a_v decreases. At $a_v \simeq 0.454$ (panel (a)) the 3-pulse state loses stability and remains unstable for $a_v \lesssim 0.454$. The solution profile at this value of a_v shows three peaks state $\Xi_3^3(\lambda_L^s)$ which is embedded in a homogeneous background state with spatially growing oscillations from the leading (right) edge towards the oscillatory tail at the back (left) edge. This situation persists at $a_v = 0.453$ (panel (b)) but with a reduced spatial growth rate; between $a_v = 0.453$ and $a_v = 0.45$ we find a transition at which the connection to the spatially unstable homogeneous state apparently changes into a connection to a small amplitude periodic background wavetrain, i.e., TW with $\lambda = \lambda_S$ in Fig. 11(c). As a_v decreases further, the fold on the Ξ_3^3 branch falls below $a = a_v^{Hopf}$ and the nonlinear dispersion relation opens a gap in the vicinity of $\lambda_c = 2\pi/k_c$, much as in Fig. 9(a). The presence of this gap is inevitable given that TW with wavelength $2\pi/k_c$ bifurcate into $a_v > a_v^{Hopf}$, i.e., there are no TW with $\lambda \sim 2\pi/k_c$ in $a_v < a_v^{Hopf}$. However, TW with wavelengths $\lambda \neq 2\pi/k_c$ do bifurcate from the homogeneous state at $a_v < a_v^{Hopf}$ and such waves may therefore be present in both $a_v < a_v^{Hopf}$ and $a_v > a_v^{Hopf}$ since they also bifurcate subcritically, i.e., in the direction of increasing a_v . We conjecture that a TW of this type, with wavelength that is commensurate with the imposed period L , may form part of the heteroclinic cycle that we believe to be responsible for the fronts connecting small and large amplitude TW in this system (panel (c)). Note in particular that the location of the fold on the Ξ_3^3 branch depends on the imposed period L , as indicated in Fig. 12(top). Specifically, the fold is located at $a_v \simeq 0.4498 \gtrsim a_v^{Hopf} \simeq 0.4497$ for $L = 200$ but at $a_v \simeq 0.4496 \lesssim a_v^{Hopf}$ for $L = 100$. The reason for this is discussed below.

To shed light on this behavior we perform a stability analysis in space of Eqs. (3) linearized about the homogeneous state:

$$\begin{pmatrix} u \\ h \\ v \\ w \\ r \end{pmatrix} - \begin{pmatrix} u_0 \\ 0 \\ v_0 \\ w_0 \\ 0 \end{pmatrix} \propto e^{\mu\xi}, \quad (6)$$

where $\xi \equiv x - ct$ is the comoving coordinate. For the 3-pulse state at $a_v = 0.45$ shown in Fig. 11(c) the speed $c \simeq 0.2937$ and the corresponding spatial eigenvalues of

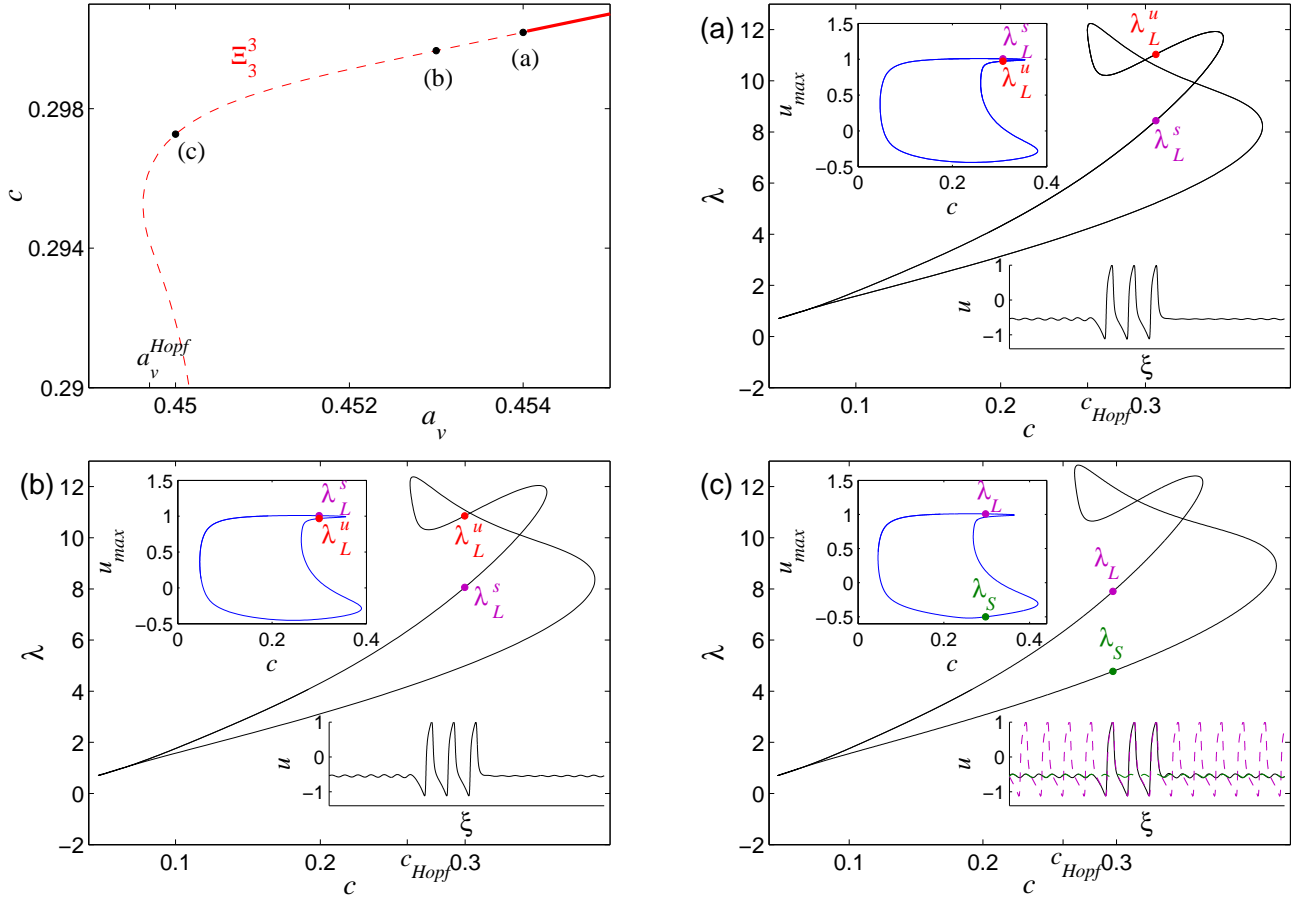


FIG. 11. (Color online) Top left panel: Zoom of the Ξ_3^3 branch near its leftmost fold at $a_v \simeq 0.4496 \lesssim a_v^{Hopf} \simeq 0.4497$, with the locations (a) $a_v = 0.454$, $c \simeq 0.3071$, (b) $a_v = 0.453$, $c \simeq 0.2997$, (c) $a_v = 0.45$, $c \simeq 0.2937$, corresponding to the pulse profiles shown in the insets in panels (a)–(c). All solutions are computed on a periodic domain with period $L = 100$; solid (dashed) lines in the top left panel indicate stable (unstable) Ξ_3^3 pulses. Panels (a)–(c) show the corresponding nonlinear dispersion relations $c(\lambda)$ for TW with wavelength λ . The computed speed c of the pulse state selects specific wavelengths from the dispersion relation: (a) $\lambda_L^s \simeq 8.4$, $\lambda_L^u \simeq 11$, (b) $\lambda_L^s \simeq 8.059$, $\lambda_L^u \simeq 10.86$, (c) $\lambda_L \simeq 7.9$, $\lambda_S \simeq 4.776$. The dashed lines in the inset in (c) correspond to TW with the wavelengths $\lambda_{L,S}$ indicated on the dispersion relation. The corresponding (c, u_{max}) plots are shown in the upper insets.

the homogeneous state are:

$$\begin{pmatrix} \mu_1 \\ \mu_2 \\ \mu_3 \\ \mu_4 \\ \mu_5 \end{pmatrix} \simeq \begin{pmatrix} -58.404 \\ -0.945 \\ 0.0037 + 1.345i \\ 0.0037 - 1.345i \\ 0.615 \end{pmatrix}. \quad (7)$$

In this type of analysis, the imaginary part of the complex eigenvalues $(\mu_{3,4})$ determines the wavenumber of weakly growing oscillations starting near \vec{U}_0 ; this wavenumber agrees with results obtained from numerical continuation [Fig. 11(c)], viz., $2\pi/\text{Im}[\mu_{3,4}] \simeq 4.67$ vs $\lambda_S \simeq 4.776$. Since $\text{Re}[\mu_{3,4}] \ll 1$, the predicted spatial growth of the oscillations is difficult to observe on domains for which $L^{-1} > \text{Re}[\mu_{3,4}]$, such as $L = 100$ [see the 3-pulse state profile in Fig. 11(c)], but becomes visible on larger domains: Figure 12(bottom) shows a 3-pulse profile in a $L = 200$ domain, also at $a_v = 0.45$, confirming the pres-

ence of the very weak amplitude growth predicted by the spatial analysis (see inset in the bottom panel), viz., $\text{Re}[\mu_{3,4}] \simeq 0.0034$ vs $\Delta \ln[u_{max}(\lambda_S) - u_0]/\Delta\xi \simeq 0.0024$. Evidently $\text{Re}[\mu_{3,4}] = 0$ at $a_v \sim a_v^{Hopf}$ although the exact location of this transition depends on the speed c of Ξ_3^3 . At this parameter value the homogeneous state of the comoving system undergoes a spatial Hopf bifurcation, shedding a periodic orbit in the direction of increasing a_v ; this periodic orbit has wave number close to $2\pi/\lambda_S$ and since the bifurcation is spatially *supercritical* this orbit will possess a weakly stable spatial Floquet multiplier. Thus the connection to the large amplitude TW is associated with an unstable Floquet multiplier of the small amplitude TW inherited from the unstable spatial eigenvalue μ_5 of \vec{U}_0 while the return to the small amplitude TW is associated with the weakly stable Floquet multiplier created at a_v^{Hopf} .

The 3-pulse states shown in Figs. 11(c) and 12(bottom)

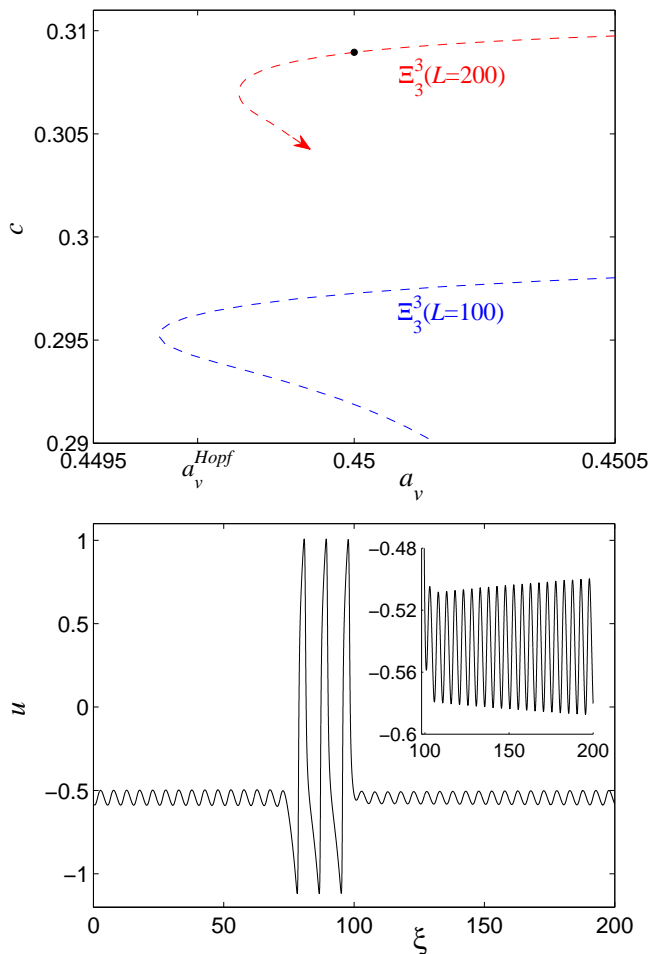


FIG. 12. (Color online) Top panel: Zoom of the Ξ_3^3 branches for $L = 100$ and $L = 200$ near their leftmost folds. The black dot marks a 3-pulse state at $a_v = 0.45$, $c \approx 0.309$, shown in the bottom panel. The inset in the bottom panel shows weak spatial growth in the oscillation amplitude that is difficult to observe on shorter domains for which $\text{Re}[\mu_{3,4}] < L^{-1}$, as in the bottom inset in Fig. 11(c).

are not the same states (Fig. 12(top)). Both solutions are periodic in space with period $L = 200$, although the state in Fig. 11(c), obtained for $L = 100$, corresponds to a weakly bound state of two groups of three pulses on a domain of length $L = 200$. Thus with $L = 200$ the two-group state (Fig. 11(c)) connects small and large amplitude TW while the one-group state (Fig. 12(bottom)) appears to connect the large amplitude TW to the homogeneous equilibrium and back again. Analysis of the standard Shil'nikov type primary homoclinic orbit to a saddle-focus shows that homoclinics corresponding to weakly bound states of two or more localized structures are present at parameter values near that corresponding to the primary homoclinic orbit [47]. Moreover, the parameter intervals with periodic orbits resembling both types of homoclinic orbits overlap, with the widths of these intervals decreasing exponentially rapidly as the

period increases [47, 54]; this is so even when these solutions travel with slightly different speeds as here. The present case is more complicated since a small amplitude periodic orbit is also present, but connections to small amplitude periodic orbits (i.e., small amplitude TW) are naturally associated with a codimension-two bifurcation called the Shil'nikov-Hopf bifurcation [55]. Our computations indicate that the parameter values of the present system are indeed quite close to such a Shil'nikov-Hopf bifurcation in space ($a_v^{Hopf} \simeq 0.4497$ vs $a_v \simeq 0.4515$ for the global connection), implying that periodic states resembling connections to the equilibrium state or to the small amplitude TW can coexist, as observed.

IV. CONCLUSION

We have reported a novel phenomenon present in excitable media: Homoclinic snaking as a mechanism for the creation of multiple stable traveling pulse trains in a three-variable system with local interactions. In addition, we have shown that the properties of finite pulse trains are reflected in the properties of the nonlinear dispersion relation relating the speed c of a periodic traveling wave to its wavelength, and indicated how the measured speed of the pulse train can be used to extract up to four relevant wavelengths from this dispersion relation. These correspond to the wavelength of the pulses within the train, the wavelength of the background small amplitude traveling wave (if present) and the wavelengths associated with the front and rear fronts connecting the pulse train to the small amplitude background traveling wave. A similar construction applies even in the case where the background traveling waves are absent and the pulse train connects to a homogeneous background state.

The finite pulse trains constructed here are of a special type – they are stationary in an appropriately moving frame, and this is so even when they connect to a background small amplitude traveling wave. This is not the only possibility, however. In other systems, for example doubly diffusive convection, stable pulses can propagate through a background TW state with a constant speed that differs from the background TW speed [54]. This type of state is not stationary in any moving frame and is associated with repeated phase slips both fore and aft. Thus while our results demonstrate that three-variable reaction-diffusion models are capable of describing a much greater variety of phenomena than the two-variable models widely employed in biology [4, 5] we anticipate that future studies will reveal yet more complex types of behavior.

ACKNOWLEDGMENTS

This work was supported in part through a grant by the Adelis foundation (AY), in part by the National Science Foundation under grant DMS-1211953

(EK), and in part by the French National Research

Agency (ANR), grant ENS-ICFP: ANR-10-238LABX-0010/ANR-10-IDEX-0001-02 PSL* (MHK).

-
- [1] M.C. Cross and P.C. Hohenberg, *Rev. Mod. Phys.* **65**, 851 (1993).
- [2] L.M. Pismen, *Patterns and Interfaces in Dissipative Dynamics* (Springer-Verlag, Berlin Heidelberg, 2006).
- [3] N. Akhmediev and A. Ankiewicz eds., *Dissipative Solitons: From Optics to Biology and Medicine, Lecture Notes in Physics* **751** (Springer-Verlag, Berlin Heidelberg, 2008).
- [4] J.D. Murray, *Mathematical Biology* (Springer-Verlag, New York, 2002).
- [5] E.M. Izhikevich *Dynamical Systems in Neuroscience: The Geometry of Excitability and Bursting* (MIT Press, Cambridge, Massachusetts, 2007).
- [6] R. Kapral and K. Showalter eds., *Chemical Waves and Patterns* (Kluwer Academic Press, Dordrecht, 1995).
- [7] I.R. Epstein and J.A. Pojman, *An Introduction to Nonlinear Chemical Dynamics: Oscillations, Waves, Patterns and Chaos* (Oxford University Press, New York, 1998).
- [8] K. Krischer, N. Mazouz, and P. Grauel, *Angewandte Chemie-International Edition* **40**, 851 (2001).
- [9] P. Couillet, T. Frisch, J.M. Gilli, and S. Rica, *Chaos* **4**, 485 (1994).
- [10] J.R. Tredicce, in *Fundamental Issues of Nonlinear Laser Dynamics*, eds. B. Krauskopf and D. Lenstra, *AIP Conf. Proc.* **548**, 238 (AIP Melville, New York, 2000).
- [11] L.L. Bonilla, *J. Phys. Cond. Matter* **14**, R341 (2002).
- [12] N.A. Vlasenko et al., *Semiconductor Physics, Quantum Electronics & Optoelectronics* **7**, 82 (2004).
- [13] M. Orlik, *J. Solid State Electrochemistry* **13**, 245 (2009).
- [14] D. Barkley, *Phys. Rev. E* **84**, 016309 (2011).
- [15] J.N. Weiss et al., *Circulation* **112**, 1232 (2005).
- [16] J.J. Tyson and J.P. Keener, *Physica D* **32**, 327 (1988).
- [17] E. Meron, *Phys. Rep.* **218**, 1 (1992).
- [18] B.N. Vasiev, *Phys. Lett. A* **323**, 194 (2004).
- [19] Y. Zeng et al., *Biophys. J.* **101**, 2122 (2011).
- [20] J. Allard and A. Mogilner, *Curr. Opin. Cell Biol.* **25**, 107 (2013).
- [21] C. Shi and P. A. Iglesias, *WIREs Syst. Biol. Med.* **5**, 631 (2013).
- [22] I. Aranson, H. Levine, and L. Tsimring, *Phys. Rev. Lett.* **76**, 1170 (1996).
- [23] C.P. Schenk, M. Or-Guil, M. Bode, and H.-G. Purwins, *Phys. Rev. Lett.* **78**, 3781 (1997).
- [24] Y. Nishiura, T. Teramoto, and K.-I. Ueda, *Chaos* **13**, 962 (2003).
- [25] P. van Heijster, A. Doelman, and T.J. Kaper, *Physica D* **237**, 3335 (2008).
- [26] L. Yang, A.M. Zhabotinsky, and I.R. Epstein, *Phys. Chem. Chem. Phys.* **8**, 4647 (2006).
- [27] A. Yochelis et al., *Europhys. Lett.* **83**, 64005 (2008).
- [28] G. Bordyugov and H. Engel, *Phys. Rev. E* **74**, 016205 (2006).
- [29] H.G.E. Meijer and S. Coombes, *EPJ Nonlinear Biomedical Physics* **2**, 3 (2014).
- [30] E. Knobloch, *Nonlinearity* **21**, T45 (2008);
- [31] A. Yochelis and A. Garfinkel, *Phys. Rev. E* **77**, 035204 (2008).
- [32] A. Yochelis, Y. Tintut, L.L. Demer, and A. Garfinkel, *New J. Phys.* **10**, 055002 (2008).
- [33] V. Breña-Medina and A. Champneys, *Phys. Rev. E* **90**, 032923 (2014).
- [34] M. Stich, Ph.D. thesis, Technische Universität Berlin (2003); M. Stich, A.S. Mikhailov, and Y. Kuramoto, *Phys. Rev. E* **79**, 026110 (2009).
- [35] A. Anma, K. Sakamoto, and T. Yoneda, *Kodai Math. J.* **35**, 215 (2012).
- [36] S. Hata, H. Nakao, and A.S. Mikhailov, *Prog. Theor. Exp. Phys.* 013A01 (2014).
- [37] E. Doedel et al., *AUTO07p: Continuation and bifurcation software for ordinary differential equations*, <http://indy.cs.concordia.ca/auto/>.
- [38] E. Knobloch, *Phys. Rev. A* **34**, 1538 (1986).
- [39] G. Röder, G. Bordyugov, H. Engel, and M. Falcke, *Phys. Rev. E* **75**, 036202 (2007)
- [40] J. Burke, S. M. Houghton, and E. Knobloch, *Phys. Rev. E* **80**, 036202 (2009).
- [41] J. Burke and E. Knobloch, *Phys. Rev. E* **73**, 056211 (2006).
- [42] W.J. Firth, L. Columbo, and A.J. Scroggie, *Phys. Rev. Lett.* **99**, 104503 (2007).
- [43] J.H.P. Dawes, *SIAM J. Appl. Dyn. Syst.* **7**, 186 (2008).
- [44] C. Beaume, H.-C. Kao, E. Knobloch and A. Bergeon, *Phys. Fluids* **25**, 124105 (2013).
- [45] A.R. Champneys et al., *SIAM J. Applied Dyn. Syst.* **6**, 663 (2007).
- [46] S.P. Hastings, *SIAM J. Appl. Math.* **42**, 247 (1982).
- [47] P. Glendinning and C.T. Sparrow, *J. Stat. Phys.* **35**, 645 (1984).
- [48] C. Elphick, E. Meron, and E.A. Spiegel, *SIAM J. Appl. Math.* **50**, 490 (1990).
- [49] C. Elphick, E. Meron, J. Rinzel, and E.A. Spiegel, *J. Theor. Biol.* **146**, 249 (1990).
- [50] M. Falcke, M. Or-Guil, and M. Bär, *Phys. Rev. Lett.* **84**, 4753 (2000).
- [51] M. Or-Guil, I.G. Kevrekidis, and M. Bär, *Physica D* **135**, 154 (2000).
- [52] N. Manz, C.T. Hamik, and O. Steinbock, *Phys. Rev. Lett.* **92**, 248301 (2004).
- [53] G. Bordyugov and H. Engel, *Phys. Rev. Lett.* **90**, 148302 (2003).
- [54] A. Spina, J. Toomre and E. Knobloch, *Phys. Rev. E* **57**, 524 (1998).
- [55] P. Hirschberg and E. Knobloch, *Physica D* **62**, 202 (1993).